HOKKAIDO UNIVERSITY

Title	Variations in initial Al-26/Al-27 ratios among fine-grained Ca-Al-rich inclusions from reduced CV chondrites
Author(s)	Kawasaki, Noriyuki; Wada, Sohei; Park, Changkun; Sakamoto, Naoya; Yurimoto, Hisayoshi
Citation	Geochimica et cosmochimica acta, 279, 1-15 https://doi.org/10.1016/j.gca.2020.03.045
Issue Date	2020-06-15
Doc URL	http://hdl.handle.net/2115/85905
Rights	©2020. This manuscript version is made available under the CC-BY-NC-ND 4.0 license http://creativecommons.org/licenses/by-nc-nd/4.0/
Rights(URL)	http://creativecommons.org/licenses/by-nc-nd/4.0/
Type	article (author version)
File Information	Geochim. Cosmochim. Acta 279_1-15.pdf

Instructions for use

1   **Variations in initial ^{26}Al/^{27}Al ratios among fine-grained Ca-Al-rich inclusions from**

2   **reduced CV chondrites**

3

4   Noriyuki Kawasaki [a,*], Sohei Wada [a], Changkun Park [b], Naoya Sakamoto [c] and Hisayoshi

5   Yurimoto [a,c,d]

6

7   *[a]Department of Natural History Sciences, Hokkaido University, Sapporo 060-0810,*

8   *Japan*

9   *[b]Division of Earth-System Sciences, Korea Polar Research Institute, Incheon 21990,*

10   *Republic of Korea*

11   *[c]Isotope Imaging Laboratory, Creative Research Institution, Hokkaido University,*

12   *Sapporo 001-0021, Japan*

13   *[d]Institute of Space and Astronautical Science, Japan Aerospace Exploration Agency,*

14   *Sagamihara 252-5210, Japan*

15

16   *Corresponding author: Noriyuki Kawasaki

17   Address: Department of Natural History Sciences, Hokkaido University, Sapporo 060-

18   0810, Japan.

19   Tel: +81-11-706-3586

20   Email: kawasaki@ep.sci.hokudai.ac.jp

21

ABSTRACT

Fine-grained Ca-Al-rich inclusions (FGIs) in CV chondrites are suggested to be condensates formed directly from the solar nebular gas. Al−Mg mineral isochrons of seven FGIs from reduced CV chondrites Efremovka, Vigarano, Thiel Mountains 07007, and Northwest Africa 8613 were obtained via *in situ* Al–Mg isotope measurements using secondary ion mass spectrometry. The slopes of the mineral isochrons for seven FGIs exhibit statistically significant variations in initial $^{26}Al/^{27}Al$ ratios, $(^{26}Al/^{27}Al)_0$, ranging from (5.19 ± 0.17) to $(3.35 \pm 0.21) \times 10^{-5}$, which correspond to a relative age spread of 0.44 ± 0.07 Myr. Inferred upper limit of $(^{26}Al/^{27}Al)_0$ for the FGIs is identical to the Solar System $(^{26}Al/^{27}Al)_0$ of $\sim 5.2 \times 10^{-5}$ as determined by whole-rock Al–Mg isochron studies for CAIs in CV chondrites. The intercepts of the mineral isochrons, the initial $^{26}Mg/^{24}Mg$ ratios the FGIs formed with, are consistent with Mg-isotope evolution path of a solar-composition nebular gas. The observed variations in $(^{26}Al/^{27}Al)_0$ for FGIs are essentially similar to those (~ 5.2 to $\sim 4.2 \times 10^{-5}$) for coarse-grained, igneous CAIs of CV chondrites that are formed by melting and solidification. If ^{26}Al was distributed homogeneously in the forming region, then our data indicate that thermal processes of condensation and melting for CAI formation occurred contemporaneously and continued for at least ~ 0.4 Myr at the very beginning of the Solar System. Alternatively, the observed variations in $(^{26}Al/^{27}Al)_0$ also indicate the possibility of heterogeneous distributions of ^{26}Al in the forming region, corresponding to a range of over at least $3.4 \times 10^{-5} < (^{26}Al/^{27}Al)_0 < 5.2 \times 10^{-5}$.

1. INTRODUCTION

Ca-Al-rich inclusions (CAIs) in chondrites are the oldest objects formed in our Solar System with an average age of 4567.30 ± 0.16 Ma as determined by U-corrected Pb–Pb absolute chronology (Connelly et al., 2012). CAIs had incorporated live-^{26}Al, a short-lived radionuclide with a half-life of 0.705 Myr (Norris et al., 1983), at the time of their formation (e.g., Lee et al., 1976; MacPherson et al., 1995). The initial ^{26}Al abundances for CAIs and other various Solar System materials can be applied to infer relative chronology of the early Solar System (e.g., Kita et al., 2013). Several studies suggested that ^{26}Al was homogeneously distributed throughout at least the region of the Solar System where "canonical" CAIs in CV chondrites formed (e.g., MacPherson et al., 1995; Jacobsen et al., 2008; Larsen et al., 2011). Conversely, heterogeneous distributions of ^{26}Al in the inner solar protoplanetary disk have also been suggested from multiple meteoritic records, (1) presence of ^{26}Al-poor refractory objects, such as FUN CAIs in CV chondrites (e.g., Wasserburg et al., 1977; Park et al., 2017 and references therein), corundum grains in carbonaceous and unequilibrated ordinary chondrites (Makide et al., 2011), grossite- and hibonite-rich CAIs in CH and CH/CB chondrites (e.g., Krot et al., 2008), and hibonite-rich CAIs with large nucleosynthetic anomalies of Ti and Ca isotopes in CM chondrites (e.g., Kööp et al., 2016 and references therein), (2) Al−Mg isotopic compositions of bulk chondrites (Larsen et al., 2011), and (3) age mismatches between U-corrected Pb−Pb and ^{26}Al–^{26}Mg systems for angrites (Schiller et al., 2015) and individual chondrules (Bollard et al., 2019).

CAIs are considered to have experienced complex thermal histories in the solar nebular gas having variable isotope compositions during the formation (e.g., Yurimoto et al., 2008; MacPherson, 2014; Krot, 2019 and references therein). Coarse-grained, igneous

68 CAIs in CV chondrites, such as compact Type A, Type B, and Type C CAIs, experienced

69 melting of precursor solids and crystallization from a melt (e.g., MacPherson and

70 Grossman, 1981; Wark and Lovering, 1982; Wark, 1987; Yurimoto et al., 1998). High-

71 precision Al–Mg mineral isochron studies using secondary ion mass spectrometry (SIMS)

72 revealed that initial $^{26}Al/^{27}Al$ ratios, $(^{26}Al/^{27}Al)_0$, for compact Type A and Type B CAIs in

73 CV chondrites range from ~5.2 to ~4.2 $\times$ 10^{-5}, which correspond to a relative formation

74 age spread of ~0.2−0.3 Myr (Kita et al., 2012; MacPherson et al., 2012, 2017, 2018;

75 Kawasaki et al., 2018). Formation events of Type C CAIs are likely related to the

76 chondrule formation and they exhibit significantly lower $(^{26}Al/^{27}Al)_0$ for their last melting

77 events, corresponding to a relative age of > ~2 Myr after formation of most CAIs (e.g.,

78 Krot et al., 2005, 2007; Kawasaki et al., 2015).

79   Coarse-grained, fluffy Type A (FTA) CAIs of CV chondrites generally exhibit

80 irregular shapes with aggregate structures and are composed mainly of gehlenitic melilite

81 (MacPherson and Grossman, 1984; Katayama et al., 2012; Kawasaki et al., 2012). They

82 do not display signatures of later extensive melting and can be formed by gas–solid

83 condensation (MacPherson and Grossman, 1984; Katayama et al., 2012; Kawasaki et al.,

84 2017). There are three FTA CAIs obtained for high-precision Al–Mg mineral isochrons

85 and they show $(^{26}Al/^{27}Al)_0$ ranging from ~5.1 to ~4.4 $\times$ 10^{-5} (MacPherson et al., 2012;

86 Kawasaki et al., 2017, 2019), which is similar to those for the igneous CAIs and

87 corresponds to a relative formation age spread of ~0.2 Myr.

88   Spinel-rich, fine-grained inclusions (FGIs) in CV chondrites are suggested as

89 condensates directly from the solar nebular gas, based on their volatility-fractionated

90 trace-element patterns (Boynton, 1975; Davis and Grossman 1979) and complex multi-

91 layered structures (Wark and Lovering, 1977; Krot et al., 2004a). Two spinel-rich FGIs in

92   CV chondrites are examined for high-precision Al–Mg mineral isochron and they exhibit

93   apparently constant $(^{26}Al/^{27}Al)_0$ of ~5.2×10^{-5} (MacPherson et al., 2010; Kawasaki et al.,

94   2019), being identical to the whole-rock CAI $(^{26}Al/^{27}Al)_0$ (Jacobsen et al., 2008; Larsen

95   et al., 2011). Given the limited number for Al–Mg data of FGIs, relationships of

96    $(^{26}Al/^{27}Al)_0$ between igneous CAIs and condensate CAIs are still poorly understood

97   although this type of an investigation enables constraining chronological relationships

98   between high-temperature thermal processes of condensation and melting of CAI

99   minerals in the earliest Solar System.

100   FGIs in the reduced CV chondrites preserve the original mineral assemblages

101   formed by condensation, which consist mainly of spinel, melilite, anorthite, and

102   aluminous diopside with more rarely perovskite and hibonite (Krot et al., 2004a), however,

103   in FGIs from oxidized CV chondrites, such as Allende, original anorthite and melilite

104   have been replaced by secondary minerals such as nepheline and sodalite (MacPherson,

105   2014). In this study, we present Al–Mg mineral isochrons for seven FGIs from reduced

106   CV chondrites, Efremovka, Vigarano, Thiel Mountains (TIL) 07007, and Northwest

107   Africa (NWA) 8613 via *in situ* isotope analysis with SIMS. The isochrons enable (1) a

108   more systematic comparison of $(^{26}Al/^{27}Al)_0$ between igneous CAIs and condensate CAIs

109   than that achieved in previous studies and (2) quantitative investigations of Mg-isotope

110   evolution of FGIs to provide constraints on a gaseous reservoir from which they

111   condensed.

112

113   **2. EXPERIMENTAL TECHNIQUES**

114   **2.1 Sample preparation and elemental analysis**

115   FGIs *HKE02* and *HKE03* are included in a polished section of Efremovka (Fig.

5

116   1), which also includes an FTA CAI *HKE01* (Kawasaki et al., 2012, 2019). An FGI

117   *HKV03* is found in a polished section of Vigarano. FGIs *TIL01*, *TIL02*, and *TIL03* are

118   found in a polished thin section of TIL 07007. An FGI *HKD01* is found in a polished

119   section of NWA 8613. The polished sections were coated with a carbon thin film (~20

120   nm) for backscattered electron (BSE) imaging, elemental analysis using an energy

121   dispersive X-ray spectrometer (EDS), and electron backscatter diffraction (EBSD)

122   mapping. Subsequently, they were coated with a gold thin film (~70 nm) for *in situ* Al−Mg

123   isotope measurements using SIMS.

124   BSE images were obtained via a field emission type scanning electron

125   microscope (FE-SEM; JEOL JSM-7000F) at Hokkaido University. Quantitative

126   elemental analysis and X-ray elemental mapping were conducted via an energy dispersive

127   X-ray spectrometer (EDS; Oxford X-Max 150) installed on the FE-SEM. A 15 keV

128   electron beam probe with currents of 1 nA (for quantitative analysis) and 10 nA (for

129   mapping) was employed in the present study. Bulk Al/Mg chemical compositions of FGIs

130   were estimated as an average of multiple measurements covering the entire CAIs via a

131   raster electron beam. We calculated ^{27}Al/^{24}Mg ratios for each FGI from the bulk Al/Mg

132   chemical compositions obtained by EDS assuming terrestrial reference ratios of

133   ^{25}Mg/^{24}Mg = 0.12663 and ^{26}Mg/^{24}Mg = 0.13932 (Catanzaro et al., 1966). Crystal

134   orientation mapping of the CAI minerals was performed via an EBSD system (AZtec

135   HKL) equipped with the FE-SEM with a 20 keV electron beam probe and a current of 4

136   nA to determine grain boundaries of each crystalline mineral. Qualitative X-ray elemental

137   mapping was simultaneously performed with EBSD crystal orientation mapping.

138   **2.2 Al−Mg isotope analysis in multicollection mode**

139   Mg-isotopes and ^{27}Al/^{24}Mg ratios of minerals in the FGIs were measured via the

140   SIMS instrument (Cameca ims-1280HR) at Hokkaido University. An ^{16}O$^-$ primary beam

141   accelerated to 23 keV was employed in the experiment. We used the peak-jumping mode

142   and multicollection mode based on the secondary ion intensities of Mg-isotopes from the

143   minerals. For the analysis of spinel and olivine, the Mg-isotopes (^{24}Mg$^+$, ^{25}Mg$^+$, and

144   ^{26}Mg$^+$) and ^{27}Al$^+$ were simultaneously measured in multicollection mode with four

145   Faraday cups: ^{24}Mg$^+$ for L2* (10^{11} Ω), ^{25}Mg$^+$ for L1 (10^{11} Ω), ^{26}Mg$^+$ for H1 (10^{11} Ω), and

146   ^{27}Al$^+$ for H2* (10^{10} Ω or 10^{11} Ω). The primary beam current was set to 0.9−4.6 nA with

147   an elliptical shape of 5×8 to 8×13 μm for spinel measurements and a 2.5 nA beam with

148   an elliptical shape of 6×10 μm was used for olivine measurements. The beam sizes are

149   comparable to or may slightly exceed crystal sizes of objective minerals in FGIs although

150   all the measurements confirmed that the sputtered craters are perfectly monomineralic.

151   The mass resolution of $M/\Delta M$ was set at ~2000. The contributions of ion interferences

152   (e.g., ^{24}MgH$^+$, ^{25}MgH$^+$, and ^{52}Cr^{2+}) were negligible under these conditions. The secondary

153   ion intensities of ^{24}Mg$^+$ were approximately $0.5−1.8 \times 10^8$ and 2.4×10^8 cps for spinel

154   and olivine, respectively. Each measurement was conducted for 20−40 cycles having a

155   counting time of 10 s. The obtained count rates were corrected for FC background and

156   relative yield of each detector. The relative sensitivity factors for aluminum and

157   magnesium were determined via measurements of Russian spinel and San Carlos olivine

158   for spinel and olivine, respectively. The δ^{25}Mg values of spinel and olivine in FGIs were

159   calculated after corrections of instrumental mass fractionation by assuming that δ^{25}Mg of

160   the Russian spinel and San Carlos olivine are zero.

161   The excess of radiogenic ^{26}Mg, δ^{26}Mg*, was calculated via an exponential

162   fractionation law with coefficient $\alpha_{natural} = 0.5128$ because natural fractionation for Mg-

163 isotopes is considered to be controlled by evaporation processes (Davis et al., 2015).

164 However, the natural mass fractionation deviates from the instrumental mass fractionation

165 of SIMS, and the instrumental mass fractionation also differs among target minerals and

166 among analytical sessions under the measurement conditions (Itoh et al., 2008; Kawasaki

167 et al., 2017, 2018, 2019). We determined instrumental mass fractionation, α_{SIMS}, via

168 measurements of terrestrial standards to calculate the excess radiogenic ^{26}Mg in each

169 analytical session. The α_{SIMS} value for spinel was determined via linear regression of the

170 Φ^{25}Mg and Φ^{26}Mg values of Takashima augite and Russian spinel, while the α_{SIMS} value

171 for olivine was determined via linear regressions of the Φ^{25}Mg and Φ^{26}Mg values of

172 Takashima augite and San Carlos olivine, where $\Phi^{25,26}$Mg $= 1000 \times$ ln

173 $[(^{25,26}\text{Mg}/^{24}\text{Mg})_{sample}/(^{25,26}\text{Mg}/^{24}\text{Mg})_{ref.}]$. The terrestrial reference ratios of $(^{25}\text{Mg}/^{24}\text{Mg})_{ref.}$

174 $= 0.12663$ and $(^{26}\text{Mg}/^{24}\text{Mg})_{ref.} = 0.13932$ (Catanzaro et al., 1966) were used for δ^{26}Mg*

175 calculations, although the final corrected-δ^{26}Mg* values are independent of the ratios

176 taken from reference. In this study, the α_{SIMS} for spinel was found to be 0.525 ± 0.004,

177 0.480 ± 0.004, 0.512 ± 0.004, 0.501 ± 0.005, and 0.515 ± 0.004 for different five sessions,

178 and the α_{SIMS} for olivine was 0.523 ± 0.005 (2σ). From the results of the linear regressions,

179 an instrumental offset for the δ^{26}Mg* values, β, which ranged from -0.43 to -0.93 with

180 2σ errors of $0.01-0.02$ depending on minerals and analytical sessions, was identified. The

181 fractionation corrected-δ^{26}Mg* values for CAI minerals were determined by the

182 following equation

$$\delta^{26}\text{Mg*} = \delta^{26}\text{Mg}_{\text{sample}} - \left[\left(1 + \frac{\delta^{25}\text{Mg}_{\text{sample}}}{1000}\right)^{\frac{1}{\alpha_{natural}}} - 1\right] \times 1000$$

$$- \beta + \left[\left(1 + \frac{\delta^{25}\text{Mg}_{\text{std}}}{1000}\right)^{\frac{1}{\alpha_{natural}}} - 1\right] \times 1000$$

$$- \left[\left(1 + \frac{\delta^{25}\text{Mg}_{\text{std}}}{1000}\right)^{\frac{1}{\alpha_{SIMS}}} - 1\right] \times 1000,$$

where $\delta^{25,26}\text{Mg}_{\text{sample}} = [(^{25,26}\text{Mg}/^{24}\text{Mg})_{\text{sample}}/(^{25,26}\text{Mg}/^{24}\text{Mg})_{\text{ref.}} - 1] \times 1000$, $\delta^{25}\text{Mg}_{\text{std}} = [(^{25}\text{Mg}/^{24}\text{Mg})_{\text{std}}/(^{25}\text{Mg}/^{24}\text{Mg})_{\text{ref.}} - 1] \times 1000$. More details and our error estimation procedure are described elsewhere (Kawasaki et al., 2017). The analytical errors (2σ) for $\delta^{26}\text{Mg*}$ were 0.09−0.10‰ for olivine and 0.09−0.18‰ for spinel.

2.4 Al−Mg isotope analysis in peak-jumping mode

For melilite and anorthite, Mg-isotopes ($^{24}\text{Mg}^+$, $^{25}\text{Mg}^+$, and $^{26}\text{Mg}^+$) were measured using an axial electron multiplier, while $^{27}\text{Al}^+$ was measured using a multicollector Faraday cup (10^{11} Ω, designed for H2*) simultaneously with $^{25}\text{Mg}^+$, in peak-jumping mode. An $^{16}\text{O}^-$ primary beam accelerated to 23 keV was employed in the experiment. The primary beam current was set to 130−140 pA with a beam size of 4−7 μm for melilite measurements and a ~180 pA beam with a beam size of ~5 μm was used for anorthite measurements. The beam sizes are comparable to or may be slightly larger than crystal sizes of objective minerals in FGIs although all the measurements confirmed that the sputtered craters are perfectly monomineralic. The mass resolution of $M/\Delta M$ was set at ~4000, which is sufficient to resolve ion interferences (e.g., $^{48}\text{Ca}^{2+}$, $^{24}\text{MgH}^+$, $^{25}\text{MgH}^+$, and $^{52}\text{Cr}^{2+}$). The secondary ion intensities of $^{24}\text{Mg}^+$ were $0.1-1.5 \times 10^5$ and $2-7 \times 10^3$ cps for melilite and anorthite, respectively. Each measurement was conducted for 100 cycles with a counting sequence with $^{24}\text{Mg}^+$ for 2 s, $^{25}\text{Mg}^+$ for 2 s, $^{25}\text{Mg}^+$ and $^{27}\text{Al}^+$ for 4 s, and

201 $^{26}Mg^+$ for 6 s. The obtained count rates were corrected for the FC background and EM

202 deadtime. The instrumental mass fractionation and relative sensitivity factors for

203 aluminum and magnesium were determined via measurements of synthetic melilite

204 glasses ($^{27}Al/^{24}Mg$ = 96 and 39) and synthetic anorthite glass ($^{27}Al/^{24}Mg$ = 330) for

205 melilite and anorthite, respectively. Details of synthetic glasses and relative sensitivity

206 factors are described partly elsewhere (Kawasaki et al., 2019). The calculation method of

207 $\delta^{26}Mg^*$ is essentially identical to those described in Section 2.3 although α_{SIMS} and β were

208 not determined in the peak-jumping mode because the instrumental mass fractionation

209 and natural mass fractionation were indistinguishable from each other under the

210 measurement conditions here. The analytical errors for $\delta^{26}Mg^*$ were assigned as internal

211 errors (2SE) and were 1.1−3.8‰ and 4.7−10.3‰ for melilite and anorthite, respectively.

212

213   **3. RESULTS**

214 **3.1 Mineralogy and petrology**

215   *HKE02* and *HKE03* are spinel-rich FGIs in the same polished section of

216 Efremovka with maximum dimensions corresponding to ~1.7 mm and ~0.9 mm,

217 respectively (Fig. 1). The FGIs are located near an FTA CAI *HKE01* (Fig. 1a; Kawasaki

218 et al., 2012, 2019). Both spinel-rich FGIs exhibit irregular shapes and similar complex

219 multi-layered textures that are mainly composed of spinel, melilite, and diopside (Fig. 2).

220 Crystal sizes of the constituent minerals are mainly a few micrometers across and

221 generally less than 10 μm across for the both spinel-rich FGIs (Figs. 2b and 2d). The

222 textures are consistent with those of previously reported spinel-rich FGIs from the

223 reduced CV chondrites (Krot et al., 2004a). The bulk $^{27}Al/^{24}Mg$ ratios of *HKE02* and

224 *HKE03* are estimated as 2.9 and 2.7, respectively. A detailed mineralogical description of

225   *HKE02* is presented by Kawasaki et al. (2019).

226   *HKV03* is a spinel-rich FGI in the polished section of Vigarano with a maximum

227   dimension of ~3 mm (Fig. 3), located near the FTA CAI *V2-01* (Katayama et al., 2012;

228   Kawasaki et al., 2017, 2019). *HKV03* exhibits a highly irregular shape and is composed

229   of nodules with multi-layered textures of spinel, melilite, and thin diopside, from their

230   core to rim (Fig 3b). Anorthite is occasionally observed between the melilite layer and

231   diopside layer. Individual nodules with sizes of several micrometers to several tens of

232   micrometers are not always directly attached to each other and are mainly separated by

233   matrix minerals. The crystal sizes of the constituent minerals are mainly a few

234   micrometers across and are generally less than 10 μm across. Hibonite and perovskite are

235   observed as accessory minerals. The bulk ^{27}Al/^{24}Mg ratio of *HKV03* could not be

236   determined owing to complex textures.

237   The reduced CV chondrite TIL 07007 contains numerous pristine FGIs (Kim and

238   Choi, 2016). *TIL01* is a spinel-rich FGI in the polished thin section of TIL 07007 with a

239   maximum dimension of ~1.3 mm (Fig. 4). On the polished thin section, *TIL01* appears as

240   being separated into two inclusions (Fig. 4a). However, the two islands are

241   petrographically very similar to each other such that they are extremely likely to

242   correspond to a single FGI. In a manner similar to the spinel-rich FGIs *HKE02* and

243   *HKE03*, *TIL01* exhibits an irregular shape and complex multi-layered textures that are

244   mainly composed of spinel, melilite, and diopside (Fig. 4b). Crystal sizes of the

245   constituent minerals are mainly a few micrometers across and generally less than 10 μm

246   across. The bulk ^{27}Al/^{24}Mg ratio of *TIL01* is estimated as 2.6.

247   *TIL02* in the polished thin section of TIL 07007 consists of fine-grained

248   anorthite-pyroxene-rich core enclosed by FTA CAI-like melilite-rich mantle, with a

249   maximum dimension of ~3.4 mm (Fig. 5). The FTA CAI-like melilite-rich mantle is

250   surrounded by a Wark–Lovering rim that is composed of spinel, anorthite, and diopside

251   (Fig. 5b, Wark and Lovering, 1977). The anorthite-pyroxene-rich core part is composed

252   of mineral layers of anorthite and diopside with fewer amounts of melilite and spinel (Figs.

253   5b and 5c). The anorthite crystals in the core part have grain sizes of typically several

254   micrometers across and generally less than 10 μm across (Figs. 5c and 5d). Spinel crystals

255   with sizes of ~1 μm are often observed in melilite crystals and at grain boundaries of

256   anorthite and melilite (Figs. 5c and 5d). The bulk $^{27}Al/^{24}Mg$ ratio of *TIL02* is estimated

257   as 5.4.

258   *TIL03* in the polished thin section of TIL 07007 is an intermediate object between

259   spinel-rich FGIs and amoeboid olivine aggregates (AOAs), with a maximum dimension

260   of ~6 mm (Fig. 6). *TIL03* exhibits an irregular shape and is petrographically divided into

261   core and mantle parts. The core part exhibits complex multi-layered textures composed

262   mainly of spinel, anorthite, diopside, and forsteritic olivine (Fig. 6b). The mantle part

263   contains melilite and more abundant olivine than the core part and olivine grains also

264   form the accretionary rim (Fig. 6c, e.g., Krot et al., 2004b). The bulk $^{27}Al/^{24}Mg$ ratio of

265   *TIL03* is estimated as 0.7. *TIL03* does not belong to either typical FGIs and AOAs and is

266   chemically intermediate between them.

267   *HKD01* in the polished thin section of NWA 8613 is a hibonite-rich FGI, which

268   exhibits an irregular shape with a maximum dimension of ~12 mm (Fig. 7). *HKD01* is

269   composed mainly of melilite, hibonite, and spinel with crystal sizes of generally less than

270   ~10 μm across with the exception of lath shaped hibonite crystals with sizes of typically

271   a few tens of micrometers. *HKD01* is petrographically divided into hibonite-spinel-rich

272   core and melilite-rich mantle parts. The entire inclusion is rimmed by a mineral layer of

12

273   hibonite, spinel and diopside. The bulk $^{27}Al/^{24}Mg$ ratio of *HKD01* is estimated as 4.8.

274   **3.2 Al−Mg isotopic compositions**

275   The Mg-isotopic compositions and $^{27}Al/^{24}Mg$ ratios measured for minerals in the

276   FGIs are summarized in Table 1 and plotted on $^{26}Al-^{26}Mg$ evolution diagrams in Fig. 8.

277   The Al–Mg isotope data of *HKE02* are obtained from Kawasaki et al. (2019). The data

278   for each FGI with the exception of *TIL02* yield very well-correlated $^{26}Al-^{26}Mg$ mineral

279   isochrons. The Al−Mg isotope data for melilite and spinel in *TIL02* plot within the error

280   on a single straight line on $^{26}Al-^{26}Mg$ evolution diagram (Fig. 8f) while the anorthite data

281   scatter significantly below the line (Fig. 8e). We define an $^{26}Al-^{26}Mg$ mineral isochron

282   of *TIL02* using melilite and spinel data (Fig. 8f) without anorthite data (see discussion

283   below). Inferred $(^{26}Al/^{27}Al)_0$ and initial $\delta^{26}Mg^*$ values, $(\delta^{26}Mg^*)_0$, for each of the FGI are

284   summarized in Table 2. The $\delta^{26}Mg^*$ data calculated using the exponent 0.511 in the

285   kinetic fractionation law (e.g., Jacobsen et al., 2008; Larsen et al., 2011; Wasserburg et

286   al., 2012) and initial values using those values are listed in supplementary materials

287   (Tables S1 and S2). The choice of exponents is insignificant for discussion in this paper

288   because the changes in $\delta^{26}Mg^*$ values and initial values are significantly lower than the

289   analytical errors.

290   Averaged $\delta^{25}Mg$ values of minerals in FGIs are 0.8 ± 2.5‰ (2SD) for melilite

291   and spinel in *HKE02*, 0.8 ± 1.9‰ for melilite and spinel in *HKE03*, 1.0 ± 1.4‰ for

292   melilite and spinel in *HKV03*, 1.1 ± 1.4‰ for melilite and spinel in *TIL01*, 0.0 ± 2.0‰

293   for melilite and spinel in *TIL02*, -2.2 ± 7.8‰ for anorthite in *TIL02*, 0.7 ± 2.1‰ for

294   melilite and olivine in *TIL03*, and 1.1 ± 2.7‰ for melilite and spinel in *HKD01*,

295   respectively. The $\delta^{25}Mg$ values of the FGI minerals are generally ~0–1‰, although those

296   of anorthite in *TIL02* exhibit large analytical errors compared with the other minerals.

297

4. DISCUSSION

4.1 Al–Mg isotope systematics

4.1.1 Disturbances of Al–Mg system for anorthite in fine-grained CAI *TIL02*

298

299

300

301   The Al–Mg systematics of *TIL02* is disturbed from a single straight line, i.e., the

302 anorthite data scatter below the mineral isochron defined by the melilite and spinel data

303 (Fig. 8e). If we estimate slopes forced through an initial Mg-isotope ratio of $\delta^{26}Mg^* = 0$

304 at $^{27}Al/^{24}Mg = 0$ for each analysis of the anorthite, then they exhibit apparent initial values

305 of $(^{26}Al/^{27}Al)_0$ ranging from $(1.1 \pm 0.5) \times 10^{-6}$ to $(1.77 \pm 0.06) \times 10^{-5}$.

306   The Al–Mg systems of anorthite in many coarse-grained CAIs from Allende,

307 Efremovka, and Vigarano are considered to have been disturbed by solid-state diffusion

308 of Mg in the anorthite after ^{26}Al decay during metamorphism on the asteroidal parent

309 body (e.g., Yurimoto et al., 2000; Fagan et al., 2007; Ito and Messenger, 2010;

310 MacPherson et al., 2012; Kawasaki et al., 2015, 2018; Aléon et al., 2018). The disturbance

311 processes of Al−Mg system for CAI minerals are controlled by the self-diffusion rates of

312 Mg in the minerals as well as their grain sizes, textural relationships, and chemical and

313 Mg-isotopic compositions within and between minerals (e.g., Yurimoto et al., 2000;

314 Kawasaki et al., 2015, 2018). Kawasaki et al. (2015) demonstrated Mg-isotope exchange

315 between anorthite and spinel resulting in resetting of the Al–Mg system for anorthite in

316 Allende Type C CAI *EK1-04-2* by quantifications of those controlling factors.

317   The anorthite measured for Al–Mg isotopes is located in the core part of *TIL02*

318 and exhibits grain sizes of typically several micrometers across and generally less than

319 10 μm across (Figs. 5c and 5d). Spinel crystals with sizes of ~1 μm are often observed at

320 grain boundaries of the anorthite. Based on the calculation by Kawasaki et al. (2015)

321   using self-diffusion coefficients of Mg-isotopes in spinel (Sheng et al., 1992; Liermann

322   and Ganguly, 2002) and in anorthite (LaTourrette and Wasserburg, 1998), if Mg-isotopes

323   in 10 μm-sized anorthite grains are equilibrated by diffusion, then Mg-isotope equilibrium

324   is also achieved in 1 μm-sized spinel grains. In order for re-equilibration of Mg-isotopes

325   in 10 μm-sized anorthite grains within a timescale of 1–10 Myr, required temperatures

326   could be calculated to be higher than ~650–700 K. The exchange conditions, textural

327   relationships, and anorthite Al–Mg isotope data suggest that the anorthite in the core part

328   of *TIL02* partially exchanged their Mg-isotopes with the spinel grains by solid-state

329   diffusion, and this could have occurred during metamorphism on the parent body, of

330   which metamorphic temperatures may have been lower than ~650–700 K. Given numbers

331   of Mg atoms in the anorthite grain and spinel grain of *TIL02*, the spinel with 1/100 volume

332   of the anorthite are sufficient to decrease $\delta^{26}Mg^{*}$ for the anorthite to 1/10. Therefore, the

333   Al–Mg isotope data for the anorthite in this study do not exhibit chronological

334   significance due to incomplete resetting of the Al–Mg system with the exception of

335   exhibiting evidence of live-^{26}Al at the CAI formation.

336   Given that the anorthite grains partially exchanged their Mg-isotopes, the

337   diffusion distance of Mg-isotopes in the spinel grains of *TIL02* may be at most 1 μm scale.

338   The spinel grains measured for Al–Mg isotopes are slightly larger than 10 μm in size, and

339   thus the Al–Mg system could have remained isotopically closed starting from their

340   formation within the measurement error. Similarly, the Al–Mg system for the melilite

341   grains measured could also have remained isotopically closed from their formation within

342   the measurement error.

343

344   **4.1.2 Primitive signatures of $(^{26}Al/^{27}Al)_{0}$ for fine-grained CAIs from reduced CV**

345 **chondrites**

346   The Al−Mg isotopic compositions of spinel and melilite in the FGIs *HKE02*,

347 *HKE03*, *HKV03*, *TIL01*, *TIL02* and *HKD01*, and olivine and melilite in the FGI *TIL03*

348 evidently exhibit an isochronous correlation between $^{27}Al/^{24}Mg$ and $\delta^{26}Mg*$. The Al−Mg

349 mineral isochrons of the seven FGIs are defined (Fig. 8). The inferred $(^{26}Al/^{27}Al)_0$ for

350 *HKE02* and *HKV03* are essentially identical to the whole-rock CAI value of $(^{26}Al/^{27}Al)_0$

351 $\sim 5.2 \times 10^{-5}$ (Jacobsen et al., 2008; Larsen et al., 2011) within their errors while those for

352 the other five FGIs are clearly lower than the whole-rock CAI value. The seven FGIs

353 exhibit statistically significant variations in $(^{26}Al/^{27}Al)_0$, ranging from (5.19 ± 0.17) to

354 $(3.35 \pm 0.21) \times 10^{-5}$.

355   The FGI *HKE02* exhibiting the highest $(^{26}Al/^{27}Al)_0$ of $(5.19 \pm 0.17) \times 10^{-5}$ and

356 FGI *HKE03* exhibiting the lowest $(^{26}Al/^{27}Al)_0$ of $(3.35 \pm 0.21) \times 10^{-5}$ are included in the

357 same polished section of Efremovka (Fig. 1). The two spinel-rich FGIs exhibit similar

358 mineralogical textures. They are composed mainly of mineral layers of spinel, melilite,

359 and diopside (Figs. 2a and 2c). The crystal sizes of the constituent minerals are mainly a

360 few micrometers across and are generally less than 10 μm across for the both FGIs (Figs.

361 2b and 2d). The re-equilibrium processes of the Al−Mg system for CAI minerals are

362 controlled by textural relationships and Al−Mg isotopic compositions of the minerals (e.g.,

363 Kawasaki et al., 2015); thus, the observations strongly suggest that the difference in

364 $(^{26}Al/^{27}Al)_0$ between them does not originate from late disturbances of the Al−Mg system

365 on the parent body. Therefore, the observed variations in $(^{26}Al/^{27}Al)_0$ among the FGIs are

366 most likely to reflect variations in $(^{26}Al/^{27}Al)_0$ acquired at nebular thermal processes (i.e.,

367 condensation) in the earliest Solar System. Similar, albeit slightly smaller, variations

368 ranging from (5.05 ± 0.18) to $(4.08 \pm 0.75) \times 10^{-5}$ were reported for individual FGIs in

369 some of the most pristine carbonaceous chondrites, Acfer 094 (C-ungrouped) and

370 Yamato-81020 (CO) (Ushikubo et al., 2017).

371

372 **4.2 $(^{26}Al/^{27}Al)_0$ and $(\delta^{26}Mg^*)_0$ for fine-grained CAIs**

373   It is still debatable whether variations in $(^{26}Al/^{27}Al)_0$ observed among CAIs

374 correspond to a formation age spread or heterogeneous distributions of $^{26}Al/^{27}Al$ ratios in

375 the forming region, or both. (e.g., Wasserburg et al., 1977; Krot et al., 2008, 2012;

376 Jacobsen et al., 2008; Larsen et al., 2011; Makide et al., 2011; Holst et al., 2015; Kööp et

377 al., 2016; Park et al., 2017; Kawasaki et al., 2019 and references therein). The debate can

378 be clarified if precisions of $(\delta^{26}Mg^*)_0$ and $(^{26}Al/^{27}Al)_0$ are sufficiently high because

379 $(\delta^{26}Mg^*)_0$ increases with time depending on the $^{26}Al/^{24}Mg$ ratio (Fig. 9). However, the

380 variations in $(\delta^{26}Mg^*)_0$ among the FGIs in this study are not resolvable even if applying

381 the smallest analytical error (0.046‰), which is one of the smallest errors for mineral

382 isochron studies so far. We cannot rule out the view of heterogeneous distributions of ^{26}Al

383 in the forming region of FGIs. If this is the case, then the data imply heterogeneous

384 distributions of ^{26}Al in the CV CAI-forming region corresponding to a range of over at

385 least $3.4 \times 10^{-5} < (^{26}Al/^{27}Al)_0 < 5.2 \times 10^{-5}$.

386   Conversely, on the Mg-isotope evolution diagram (Fig. 9), the data of FGIs plot

387 on the Mg-isotope evolution curve of solar-composition gas within the errors, thereby

388 suggesting that their $(^{26}Al/^{27}Al)_0$ correspond to a formation age spread and their

389 condensation occurred from the solar-composition nebular gas. The FGIs cannot be

390 formed via recondensation of their evaporation gas or from Al/Mg fractionated nebular

391 gas formed at the age corresponding $(^{26}Al/^{27}Al)_0$ of ~5.2×10^{-5} (Jacobsen et al., 2008;

392 Larsen et al., 2011) because the FGI data clearly deviate from the Mg-isotope evolution

393   curves of the fractionated Al/Mg ratio materials (Fig. 9). Note that the heterogeneity of

394     $^{26}Mg/^{24}Mg$ in the CAI-forming region has also been suggested (e.g., Wasserburg et al.,

395   2012; Larsen et al., 2020). The inferred $(\delta^{26}Mg*)_0$ for formation reservoirs of some of CV

396   CAIs and CAIs of CR chondrites, –0.095 ± 0.026‰ (Larsen et al., 2020), is lower than

397   that for most of CV CAIs, –0.0159 ± 0.0014‰ (Larsen et al., 2011) or –0.040 ± 0.029‰

398   (Jacobsen et al., 2008). Assuming precursors of the FGIs formed when $^{26}Al/^{27}Al$ was

399     $(5.23 ± 0.13) \times 10^{-5}$ (Jacobsen et al., 2008), the precursor $(\delta^{26}Mg*)_0$ can be back-

400   calculated to be –0.29 ± 0.13‰ for *HKE03*, –0.18 ± 0.14‰ for *TIL01*, –0.28 ± 0.13‰ for

401   *TIL02,* –0.07 ± 0.06‰ for *TIL03*, and –0.20 ± 0.09‰ for *HKD01*. Some of the back-

402   calculated $(\delta^{26}Mg*)_0$ are clearly lower than the any inferred $(\delta^{26}Mg*)_0$ values for CAI-

403   formation reservoirs above. Rather, such large negative $(\delta^{26}Mg*)_0$ values have been

404   recognized only for FUN CAIs (e.g., Park et al., 2017 and references therein), although

405   the observed variations of mass-dependent magnesium isotope fractionation for the FGIs

406   are very small ($\delta^{25}Mg \sim$ 0–1‰). These simulations further support Al/Mg chemical

407   fractionation events for the FGIs did not occur at the formation age of canonical CAIs

408   and they formed from the evolved solar-composition nebular gas (Fig. 9). The formation

409   age spread corresponds to 0.44 ± 0.07 Myr at the very beginning of the Solar System.

410   The variations in $(^{26}Al/^{27}Al)_0$ observed among the FGIs in this study are

411   essentially similar to those for coarse-grained, igneous CAIs and FTA CAIs in CV

412   chondrites (Fig. 10; Kita et al., 2012; MacPherson et al., 2012, 2017, 2018; Kawasaki et

413   al., 2017, 2018, 2019). Among them, the igneous CAIs can potentially have a significant

414   age spread, given that the relative age of the Allende Type B1 CAI TS34 from the

415   formation of canonical CAIs (Jacobsen et al., 2008; Larsen et al., 2011) calculated from

416     $(^{26}Al/^{27}Al)_0$ is consistent with the relative age calculated from $(\delta^{26}Mg*)_0$ and bulk

417    $^{27}Al/^{24}Mg$ (Kawasaki et al., 2018). Moreover, igneous CAIs exhibiting sub-canonical

418    $(^{26}Al/^{27}Al)_0$ values display elevated positive $(\delta^{26}Mg^*)_0$ values (MacPherson et al. 2012;

419   Kita et al., 2012). Therefore, if the formation regions of FGIs, igneous CAIs, and FTA

420   CAIs in CV chondrites are identical, then our data indicate that the CV CAI formation

421   continued for at least ~0.4 Myr at the very beginning of the Solar System. The inferred

422   period for the CV CAI formation can indicate either the time duration of refractory dust

423   transportation processes from the CAI-forming region, which may correspond to the inner

424   edge of the solar protoplanetary disk (Itoh and Yurimoto, 2003; Yurimoto et al., 2008), to

425   a forming region of the CV chondrite parent body (e.g., Ciesla, 2010) or the time duration

426   of occurrence of the CAI formation processes in the CAI-forming region.

427

428   <div align="center">**5. CONCLUSIONS**</div>

429   In this study, high-precision Al−Mg mineral isochrons of seven FGIs from the

430   reduced CV chondrites via *in situ* analysis with SIMS exhibited statistically significant

431   variations in $(^{26}Al/^{27}Al)_0$ among FGIs, ranging from (5.19 ± 0.17) to $(3.35 \pm 0.21) \times 10^{-5}$.

432   Two spinel-rich FGIs from Efremovka with similar mineralogical textures exhibit a

433   highest $(^{26}Al/^{27}Al)_0$ of $(5.19 \pm 0.17) \times 10^{-5}$ and a lowest $(^{26}Al/^{27}Al)_0$ of $(3.35 \pm 0.21) \times$

434   10^{-5}. This indicates that the difference in $(^{26}Al/^{27}Al)_0$ between them does not originate

435   from late disturbances of the Al−Mg system on the parent body. The inferred $(\delta^{26}Mg^*)_0$

436   values for FGIs are consistent with the Mg-isotope evolution of a solar-composition

437   nebular gas. The Al–Mg data indicate that the FGIs formed from the solar-composition

438   nebular gas over the period of 0.44 ± 0.07 Myr under the assumption of homogeneous

439   distributions of ^{26}Al in the forming region. The observed variations in $(^{26}Al/^{27}Al)_0$ for

440   FGIs are essentially similar to those for igneous CAIs in CV chondrites, thereby

441   indicating that CAIs in CV chondrites have variations in $(^{26}Al/^{27}Al)_0$ from ~5.2 to ~3.4 $\times$

442   10^{-5} despite their petrologic types and the formation processes they experienced. The data

443   indicate that CAI-formation thermal processes—condensation and melting—occurred

444   contemporaneously during ~0.4 Myr at the very beginning of the Solar System, if ^{26}Al

445   was distributed homogeneously in the forming region. Alternatively, the observed

446   variations in $(^{26}Al/^{27}Al)_0$ indicate the possibility of heterogeneous distributions of ^{26}Al in

447   the forming region, corresponding to a range of over at least $3.4 \times 10^{-5} < (^{26}Al/^{27}Al)_0 <$

448   5.2×10^{-5}.

449

455

456

457 **REFERENCES**

458 Aléon J., Marin-Carbonne J., McKeegan K. D. and El Goresy A. (2018) O, Mg, and Si

459   isotope distributions in the complex ultrarefractory CAI Efremovka 101.1:

460   Assimilation of ultrarefractory, FUN, and regular CAI precursors. *Geochimica et*

461   *Cosmochimica Acta* **232**, 48–81.

462 Bollard J., Kawasaki N., Sakamoto N., Olsen M., Itoh S., Larsen K., Wielandt D., Schiller

463   M., Connelly J. N., Yurimoto H. and Bizzarro M. (2019) Combined U-corrected

464   Pb-Pb dating and ^{26}Al-^{26}Mg systematics of individual chondrules – Evidence for

465   a reduced initial abundance of ^{26}Al amongst inner Solar System chondrules.

466   *Geochimica et Cosmochimica Acta* **260**, 62–83.

467 Boynton W. V. (1975) Fractionation in the solar nebula—Condensation of yttrium and

468   the rare earth elements. *Geochimica et Cosmochimica Acta* **39**, 569–584.

469 Catanzaro E. J., Murphy T. J., Garner E. L. and Shields W. R. (1966) Absolute isotopic

470   abundance ratios and atomic weights of magnesium. *J. Res. natl. Bur Stand.* **70a**,

471   453–458.

472 Ciesla F. J. (2010) The distributions and ages of refractory objects in the solar nebula.

473   *Icarus* **208**, 455–467.

474 Connelly J. N., Bizzarro M., Krot A. N., Nordlund Å., Wielandt D. and Ivanova M. A.

475   (2012) The absolute chronology and thermal processing of solids in the solar

476   protoplanetary disk. *Science* **338**, 651–655.

477 Davis A. M. and Grossman L. (1979) Condensation and fractionation of rare earths in the

478   solar nebula. *Geochimica et Cosmochimica Acta* **43**, 1611–1632.

479 Davis A. M., Richter F. M., Mendybaev R. A., Janney P. E., Wadhwa M. and McKeegan

480   K. D. (2015) Isotopic mass fractionation laws for magnesium and their effects on

481   ^{26}Al–^{26}Mg systematics in solar system materials. *Geochimica et Cosmochimica*

482   *Acta* **158**, 245–261.

483 Fagan T. J., Guan Y. and MacPherson G. J. (2007) Al-Mg isotopic evidence for episodic

484   alteration of Ca-Al-rich inclusions from Allende. *Meteoritics & Planetary Science*

485   **42**, 1221–1240.

486 Holst J. C., Olsen M. B., Paton C., Nagashima K., Schiller M., Wielandt D., Larsen K. K.,

487   Connelly J. N., Jorgensen J. K., Krot A. N., Nordlund A. and Bizzarro M. (2013)

488   ^{182}Hf-^{182}W age dating of a ^{26}Al-poor inclusion and implications for the origin of

489   short-lived radioisotopes in the early Solar System. *Proceedings of the National*

490   *Academy of Sciences of the United States of America* **110**, 8819–8823.

491 Ito M. and Messenger S. (2010) Thermal metamorphic history of a Ca, Al-rich inclusion

492   constrained by high spatial resolution Mg isotopic measurements with NanoSIMS

493   50L. *Meteoritics & Planetary Science* **45**, 583–595.

494 Itoh S. and Yurimoto H. (2003) Contemporaneous formation of chondrules and refractory

495   inclusions in the early solar system. *Nature* **423**, 728−731.

496 Itoh S., Makide K. and Yurimoto H. (2008) Calculation of radiogenic ^{26}Mg of CAI

497   minerals under high precision isotope measurement by SIMS. *Applied Surface*

498   *Science* **255**, 1476–1478.

499 Jacobsen B., Yin Q., Moynier F., Amelin Y., Krot A. N., Nagashima K., Hutcheon I. D.

500   and Palme H. (2008) ^{26}Al-^{26}Mg and ^{207}Pb-^{206}Pb systematics of Allende CAIs:

501   Canonical solar initial ^{26}Al/^{27}Al ratio reinstated. *Earth and Planetary Science*

502   *Letters* **272**, 353–364.

503 Katayama J., Itoh S. and Yurimoto H. (2012) Oxygen isotopic zoning of reversely zoned

504   melilite crystals in a Fluffy Type A Ca-Al-rich inclusion from the Vigarano

505   meteorite. *Meteoritics & Planetary Science* **47**, 2094–2106.

506 Kawasaki N., Sakamoto N. and Yurimoto H. (2012) Oxygen isotopic and chemical zoning

507   of melilite crystals in a Type A Ca-Al-rich inclusion of Efremovka CV3 chondrite.

508   *Meteoritics & Planetary Science* **47**, 2084–2093.

509 Kawasaki N., Kato C., Itoh S., Wakaki S., Ito M. and Yurimoto H. (2015) ^{26}Al–^{26}Mg

510   chronology and oxygen isotope distributions of multiple melting for a Type C CAI

511   from Allende. *Geochimica et Cosmochimica Acta* **169**, 99–114.

512 Kawasaki N., Itoh S., Sakamoto N. and Yurimoto H. (2017) Chronological study of

513   oxygen isotope composition for the solar protoplanetary disk recorded in a fluffy

514   Type A CAI from Vigarano. *Geochimica et Cosmochimica Acta* **201**, 83–102.

515 Kawasaki N., Simon S. B., Grossman L., Sakamoto N. and Yurimoto H. (2018) Crystal

516   growth and disequilibrium distribution of oxygen isotopes in an igneous Ca-Al-

517   rich inclusion from the Allende carbonaceous chondrite. *Geochimica et*

518   *Cosmochimica Acta* **221**, 318–341.

519 Kawasaki N., Park C., Sakamoto N., Park S. Y., Kim H. N., Kuroda M. and Yurimoto H.

520   (2019) Variations in initial ^{26}Al/^{27}Al ratios among fluffy Type A Ca–Al-rich

521   inclusions from reduced CV chondrites. *Earth and Planetary Science Letters* **511**,

522   25–35.

523 Kim H. and Choi B.-G. (2016) Petrological characteristics of the fine-grained CAIs from

524   the reduced CV chondrites Thiel Mountains 07003 and 07007, and origin of

525   anorthite. (abstract #6290) In: 79th Annual Meeting of the Meteoritical Society.

526 Kita N. T., Ushikubo T., Knight K. B., Mendybaev R. A., Davis A. M., Richter F. M. and

527   Fournelle J. H. (2012) Internal ^{26}Al-^{26}Mg isotope systematics of a Type B CAI:

528   Remelting of refractory precursor solids. *Geochimica et Cosmochimica Acta* **86**,

529   37–51.

530 Kita N. T., Yin Q.-Z., MacPherson G. J., Ushikubo T., Jacobsen B., Nagashima K.,

531   Kurahashi E., Krot A. N. and Jacobsen S. B. (2013) [26]Al-[26]Mg isotope systematics

532   of the first solids in the early solar system. *Meteoritics & Planetary Science* **48**,

533   1383–1400.

534 Kööp L., Davis A. M., Nakashima D., Park C., Krot A. N., Nagashima K., Tenner T. J.,

535   Heck P. R. and Kita N. T. (2016) A link between oxygen, calcium and titanium

536   isotopes in [26]Al-poor hibonite-rich CAIs from Murchison and implications for the

537   heterogeneity of dust reservoirs in the solar nebula. *Geochimica et Cosmochimica*

538   *Acta* **189**, 70–95.

539 Krot A. N., MacPherson G. J., Ulyanov A. A. and Petaev M. I. (2004a) Fine-grained,

540   spinel-rich inclusions from the reduced CV chondrites Efremovka and Leoville: I.

541   Mineralogy, petrology, and bulk chemistry. *Meteoritics & Planetary Science* **39**,

542   1517–1553.

543 Krot A. N., Petaev M. I., Russell S. S., Itoh S., Fagan T. J., Yurimoto H., Chizmadia L.,

544   Weisberg M. K., Komatsu M., Ulyanov A. A. and Keil K. (2004b) Amoeboid

545   olivine aggregates and related objects in carbonaceous chondrites: records of

546   nebular and asteroid processes. *Chemie der Erde* **64**, 185–239.

547 Krot A. N., Yurimoto H., Hutcheon I. D. and MacPherson G. J. (2005) Chronology of the

548   early Solar System from chondrule-bearing calcium-aluminium-rich inclusions.

549   *Nature* **434**, 998−1001.

550 Krot A. N., Yurimoto H., Hutcheon I. D., Chaussidon M., MacPherson G. J. and Paque J.

551   (2007) Remelting of refractory inclusions in the chondrule-forming regions:

552   Evidence from chondrule-bearing type C calcium-aluminum-rich inclusions from

553   Allende. *Meteoritics & Planetary Science* **42**, 1197−1219.

554 Krot A. N., Nagashima K., Bizzarro M., Huss G. R., Davis A. M., McKeegan K. D.,

555   Meyer B. S. and Ulyanov A. A. (2008) Multiple generations of refractory inclusions

556   in the metal-rich carbonaceous chondrites Acfer 182/214 and Isheyevo. *The*

557   *Astrophysical Journal* **672**, 713–721.

558 Krot A. N., Makide K., Nagashima K., Huss G. R., Ogliore R. C., Ciesla F. J., Yang L.,

559   Hellebrand E. and Gaidos E. (2012) Heterogeneous distribution of ^{26}Al at the birth

560   of the solar system: Evidence from refractory grains and inclusions. *Meteoritics*

561   *& Planetary Science* **47**, 1948–1979.

562 Krot A. N. (2019) Refractory inclusions in carbonaceous chondrites: Records of early

563   solar system processes. *Meteoritics & Planetary Science* **54**, 1647–1691.

564 Larsen K. K., Trinquier A., Paton C., Schiller M., Wielandt D., Ivanova M. A., Connelly

565   J. N., Nordlund Å., Krot A. N. and Bizzarro M. (2011) Evidence for magnesium

566   isotope heterogeneity in the solar protoplanetary disk. *The Astrophysical Journal*

567   *Letters* **735**, L37–L43.

568 Larsen K. K., Wielandt D., Schiller M., Krot A. N. and Bizzarro M. (2020) Episodic

569   formation of refractory inclusions in the Solar System and their presolar heritage.

570   *Earth and Planetary Science Letters* **535**, 116088.

571 LaTourrette T. and Wasserburg G. J. (1998) Mg diffusion in anorthite: implications for

572   the formation of early solar system planetesimals. *Earth and Planetary Science*

573   *Letters* **158**, 91–108.

574 Lee T., Papanastassiou D. A. and Wasserburg G. J. (1976) Demonstration of Mg-26 excess

575   in Allende and evidence for Al-26. *Geophysical Research Letters* **3**, 41–44.

576 Liermann H.-P. and Ganguly J. (2002) Diffusion kinetics of Fe^{2+} and Mg in aluminous

577   spinel: Experimental determination and applications. *Geochimica et*

578   *Cosmochimica Acta* **66**, 2903–2913.

579 Lodders K. (2003) Solar system abundances and condensation temperatures of the

580   elements. *The Astrophysical Journal* **591**, 1220–1247.

581 Ludwig K. (2003) ISOPLOT: A Geochronological Toolkit for Microsoft Excel 3.00.

582   Berkeley Geochronological Center Special Publication No. 4, Berkeley, CA 94709.

583 MacPherson G. J. and Grossman L. (1981) A once-molten, coarse-grained, Ca-rich

584   inclusion in Allende. *Earth and Planetary Science Letters* **52**, 16–24.

585 MacPherson G. J. and Grossman L. (1984) Fluffy Type A Ca-, Al-rich inclusions in the

586   Allende meteorite. *Geochimica et Cosmochimica Acta* **48**, 29−46.

587 MacPherson G. J., Davis A. M. and Zinner E. K. (1995) The distribution of aluminum-26

588   in the early Solar System-A reappraisal. *Meteoritics* **30**, 365–386.

589 MacPherson G. J., Bullock E. S., Janney P. E., Kita N. T., Ushikubo T., Davis A. M.,

590   Wadhwa M. and Krot A. N. (2010) Early solar nebular condensates with canonical,

591   not supracanonical, initial ^{26}Al/^{27}Al ratios. *The Astrophysical Journal Letters* **711**,

592   L117–L121.

593 MacPherson G. J., Kita N. T., Ushikubo T., Bullock E. S. and Davis A. M. (2012) Well-

594   resolved variations in the formation ages for Ca-Al-rich inclusions in the early

595   Solar System. *Earth and Planetary Science Letters* **331**–**332**, 43–54.

596 MacPherson G. J. (2014) Calcium-aluminum-rich inclusions in chondritic meteorites. In

597   *Meteorites and Cosmochemical Processes*, edited by Davis A. M. Treatise on

598   Geochemistry vol. 1, Elsevier, Oxford, 139–179.

599 MacPherson G. J., Bullock E. S., Tenner T. J., Nakashima D., Kita N. T., Ivanova M. A.,

600   Krot A. N., Petaev M. I. and Jacobsen S. B. (2017) High precision Al–Mg

601   systematics of forsterite-bearing Type B CAIs from CV3 chondrites. *Geochimica*

602   *et Cosmochimica Acta* **201**, 65–82.

603   MacPherson G. J., Defouilloy C. and Kita N. T. (2018) High-precision Al–Mg isotopic

604   systematics in USNM 3898 – The benchmark "ALL" for initial ^{87}Sr/^{86}Sr in the

605   earliest Solar System. *Earth and Planetary Science Letters* **491**, 238-243.

606   Makide K., Nagashima K., Krot A. N., Huss G. R., Ciesla F. J., Hellebrand E., Gaidos E.

607   and Yang L. (2011) Heterogeneous distribution of ^{26}Al at the birth of the solar

608   system. *The Astrophysical Journal Letters* **733**, L31–L34.

609   Norris T. L., Gancarz A. J., Rokop D. J. and Thomas K. W. (1983) Half-life of ^{26}Al. *J.*

610   *Geophys. Res.* **88**, B331–B333.

611   Park C., Nagashima K., Krot A. N., Huss G. R., Davis A. M. and Bizzarro M. (2017)

612   Calcium-aluminum-rich inclusions with fractionation and unidentified nuclear

613   effects (FUN CAIs): II. Heterogeneities of magnesium isotopes and ^{26}Al in the

614   early Solar System inferred from in situ high-precision magnesium-isotope

615   measurements. *Geochimica et Cosmochimica Acta* **201**, 6–24.

616   Schiller M., Connelly J. N., Glad A. C., Mikouchi T. and Bizzarro M. (2015) Early

617   accretion of protoplanets inferred from a reduced inner solar system ^{26}Al inventory.

618   *Earth and Planetary Science Letters* **420**, 45–54.

619   Sheng Y. J., Wasserburg G. J. and Hutcheon I. D. (1992) Self-diffusion of magnesium in

620   spinel and in equilibrium melts: Constraints on flash heating of silicates.

621   *Geochimica et Cosmochimica Acta* **56**, 2535–2546.

622   Ushikubo T., Tenner T. J., Hiyagon H. and Kita N. T. (2017) A long duration of the ^{16}O-

623   rich reservoir in the solar nebula, as recorded in fine-grained refractory inclusions

624   from the least metamorphosed carbonaceous chondrites. *Geochimica et*

625   *Cosmochimica Acta* **201**, 103–122.

626   Wark D. A. and Lovering J. F. (1977) Marker events in the early solar system: evidence

627   from rims on Ca-Al-rich inclusions in carbonaceous chondrites. Proceedings, 8th

628   Lunar and Planetary Science Conference. pp. 95–112.

629   Wark D. A. and Lovering J.F. (1982) The nature and origin of type B1 and B2 Ca-Al-rich

630   inclusions in the Allende meteorite. *Geochimica et Cosmochimica Acta* **46**, 2581–

631   2594.

632   Wark D. A. (1987) Plagioclase-rich inclusions in carbonaceous chondrite meteorites:

633   liquid condensates? *Geochimica et Cosmochimica Acta* **51**, 221–242.

634   Wasserburg G. J., Lee T. and Papanastassiou D. A. (1977) Correlated O and Mg isotopic

635   anomalies in Allende inclusions: II. Magnesium. *Geophysical Research Letters* **4**,

636   299–302.

637   Wasserburg G. J., Wimpenny J. and Yin Q.-Z. (2012) Mg isotopic heterogeneity, Al-Mg

638   isochrons, and canonical $^{26}Al/^{27}Al$ in the early solar system. *Meteoritics &*

639   *Planetary Science* **47**, 1980–1997.

640   Yurimoto H., Ito M. and Nagasawa H. (1998) Oxygen isotope exchange between

641   refractory inclusion in Allende and solar nebula gas. *Science* **282**, 1874–1877.

642   Yurimoto H., Koike O., Nagahara H., Morioka M. and Nagasawa H. (2000)

643   Heterogeneous distribution of Mg isotopes in anorthite single crystal from Type-

644   B CAIs in Allende meteorite. (abstract #1593). In: 31st Lunar and Planetary

645   Science Conference.

646   Yurimoto H., Krot N. K., Choi B., Aléon J., Kunihiro T. and Brearley A. J. (2008) Oxygen

647   isotopes in chondritic components. In *Oxygen in the Solar System,* edited by

648   MacPherson G. J. Reviews in Mineralogy and Geochemistry, vol. 68. Washington,

649   D. C.: Mineralogical Society of America. pp. 141–186.

650

TABLES

Table 1. Magnesium isotopic compositions (‰) and $^{27}Al/^{24}Mg$ ratios of minerals in fine-grained CAIs.

Minerals	$^{27}Al/^{24}Mg$	2σ	$\delta^{26}Mg^*$	2σ	$\delta^{25}Mg$	2σ	Minerals	$^{27}Al/^{24}Mg$	2σ	$\delta^{26}Mg^*$	2σ	$\delta^{25}Mg$	2σ
HKE03							An	3855	121	38.3	10.3	-5.5	5.3
Mel	29.2	0.3	7.5	1.3	2.1	1.7	Mel	29.3	0.1	10.2	1.3	-0.3	1.1
Mel	40.8	1.1	9.9	1.5	-0.1	1.8	Mel	57.8	0.2	18.2	1.9	0.1	1.4
Mel	49.7	0.3	11.8	1.8	0.4	1.8	Mel	24.1	0.1	8.1	1.4	0.2	1.2
Mel	46.6	0.6	12.2	1.6	-0.5	1.3	Mel	48.8	0.2	16.6	1.7	-0.4	1.3
Mel	32.9	0.4	7.3	1.4	2.0	1.1	Mel	45.4	0.3	15.5	1.7	-2.5	1.2
Mel	28.8	0.3	6.6	1.2	0.7	0.8	Mel	55.3	0.3	17.5	1.4	0.0	1.2
Mel	56.1	0.6	13.7	1.5	0.7	1.3	Mel	21.6	0.1	6.6	1.1	0.9	1.1
Sp	2.582	0.004	0.69	0.11	1.05	0.06	Mel	22.5	0.1	7.0	1.1	0.8	1.3
							Mel	40.0	0.3	12.6	1.9	-0.6	1.5
HKV03							Sp	2.495	0.002	0.81	0.09	0.85	0.08
Mel	51.9	1.4	18.9	2.0	0.8	1.2	Sp	2.486	0.001	0.78	0.09	0.79	0.10
Mel	32.0	0.3	11.3	1.6	1.2	1.0							
Mel	82.8	3.3	31.1	2.4	1.1	1.3	*TIL03*						
Mel	40.3	0.5	14.5	1.9	2.3	1.3	Mel	42.6	0.7	13.1	1.9	-0.1	1.4
Mel	56.5	0.9	20.3	1.7	0.0	1.1	Mel	22.7	0.1	5.6	1.5	2.3	1.3
Mel	133.0	2.3	46.8	3.2	0.8	2.0	Mel	30.6	0.3	8.8	1.4	0.2	1.1
Mel	57.7	1.1	20.6	1.9	2.2	1.4	Mel	55.4	1.0	16.1	1.8	2.8	1.2
Mel	62.2	0.5	21.3	2.2	0.5	1.4	Mel	14.2	0.0	4.4	1.1	1.2	0.9
Sp	2.513	0.004	0.92	0.13	0.79	0.09	Mel	31.4	0.2	9.8	1.2	0.9	1.0
Sp	2.519	0.004	0.93	0.18	0.78	0.09	Mel	40.4	0.9	11.6	1.2	0.7	0.9
Sp	2.530	0.004	0.85	0.13	1.03	0.09	Ol	0.0009	0.0001	0.02	0.09	-0.39	0.07
Sp	2.503	0.004	0.80	0.14	0.26	0.10	Ol	0.0001	0.0000	-0.03	0.09	-0.09	0.05
							Ol	0.0002	0.0000	-0.03	0.09	0.17	0.05
TIL01							Ol	0.0002	0.0000	0.00	0.10	0.10	0.06
Mel	21.7	0.5	6.1	1.3	-0.5	1.1							
Mel	18.0	0.4	5.3	1.1	1.1	1.0	*HKD01*						
Mel	28.1	0.1	8.5	2.0	1.3	1.3	Mel	225.1	3.9	76.5	3.2	1.2	1.6
Mel	30.1	0.5	9.8	1.7	1.2	1.4	Mel	272.7	0.7	95.9	3.8	3.0	2.2
Mel	34.6	0.5	11.5	1.3	0.9	1.3	Mel	152.6	0.4	52.7	2.5	-0.5	1.2
Mel	19.2	0.1	5.6	1.1	2.1	1.3	Mel	139.7	1.2	47.7	2.9	2.9	2.0
Mel	26.8	0.1	9.0	1.3	0.9	1.3	Mel	59.5	0.6	19.8	1.7	-0.9	1.7
Sp	2.584	0.009	0.73	0.14	1.18	0.08	Mel	61.4	0.2	21.6	1.9	-0.5	1.7
Sp	2.591	0.009	0.84	0.12	1.49	0.07	Mel	145.6	2.4	51.0	2.5	0.9	1.3
							Mel	120.2	0.5	41.7	2.4	1.3	1.2
TIL02							Mel	85.3	0.2	27.9	2.5	0.8	1.9
An	1839	48	234.2	8.1	2.2	3.9	Sp	2.521	0.002	0.82	0.11	0.45	0.15
An	3415	131	46.5	9.0	1.5	5.5	Sp	2.518	0.002	0.81	0.14	0.09	0.14
An	1050	19	8.2	4.7	-6.2	2.8	Sp	2.506	0.001	0.75	0.12	2.55	0.15
An	1436	32	60.0	5.6	-3.1	3.3	Sp	2.512	0.001	0.85	0.11	2.62	0.15

An: anorthite, Mel: melilite, Ol: olivine, Sp: spinel

656 Table 2. Summary of $(^{26}Al/^{27}Al)_0$, $(\delta^{26}Mg^*)_0$ and bulk $^{27}Al/^{24}Mg$ for each fine-grained

657 CAI.

CAI	Meteorite	$(^{26}Al/^{27}Al)_0$	2σ	$(\delta^{26}Mg^*)_0$	2σ	bulk $^{27}Al/^{24}Mg$
HKE02[a]	Efremovka	5.19×10^{-5}	0.17×10^{-5}	0.022	0.087	2.9
HKE03	Efremovka	3.35×10^{-5}	0.20×10^{-5}	0.07	0.12	2.7
HKV03	Vigarano	4.99×10^{-5}	0.17×10^{-5}	-0.030	0.078	n.a.
TIL01	Thiel Mountains 07007	4.43×10^{-5}	0.31×10^{-5}	-0.03	0.12	2.6
TIL02	Thiel Mountains 07007	4.53×10^{-5}	0.18×10^{-5}	-0.014	0.076	5.4
TIL03	Thiel Mountains 07007	4.09×10^{-5}	0.22×10^{-5}	-0.013	0.046	0.7
HKD01	Northwest Africa 8613	4.812×10^{-5}	0.089×10^{-5}	-0.060	0.063	4.8

658 [a] From Kawasaki et al. (2019a), n.a.: not analyzed.

659
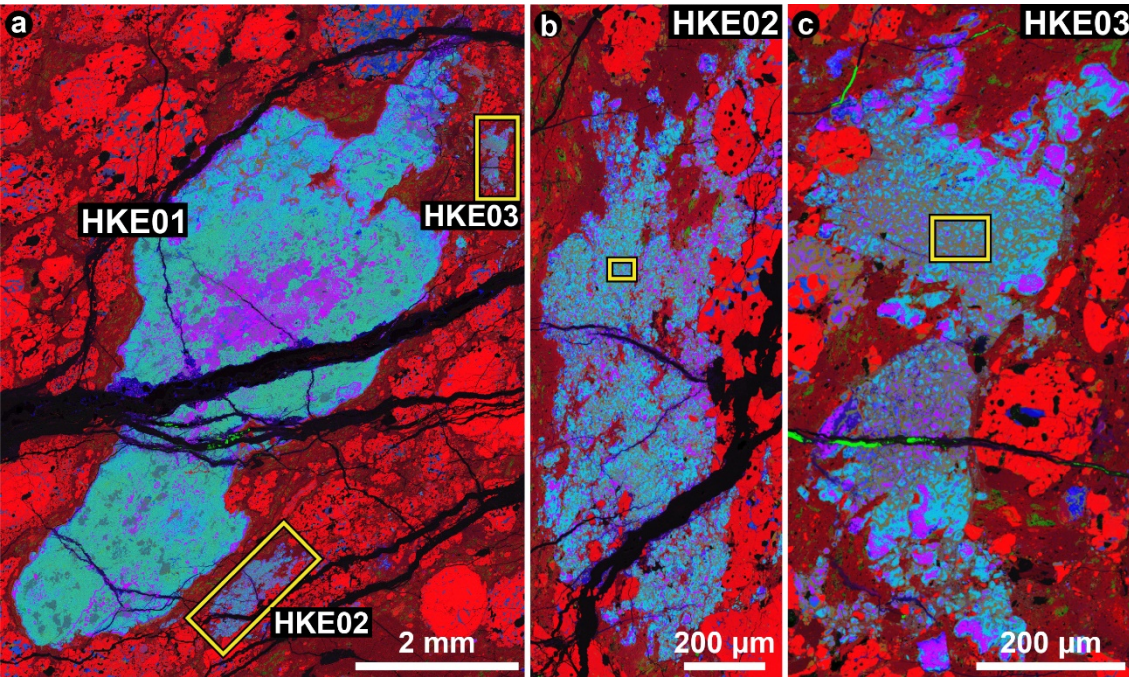
FIGURES

Figure 1. Combined X-ray elemental map of (a) fluffy Type A CAI *HKE01*, (b) fine-grained CAI *HKE02* and (c) fine-grained CAI *HKE03* from Efremovka. Mg is denoted in red, Ca is denoted in green, and Al is denoted in blue. The yellow boxes in (a) indicate the areas shown in (b) and (c). The yellow box in (b) indicates the area shown in Figs 2a and 2b. The yellow box in (c) indicates the area shown in Figs. 2c and 2d. Corresponding back scattered electron images are shown in Fig. S1.

669
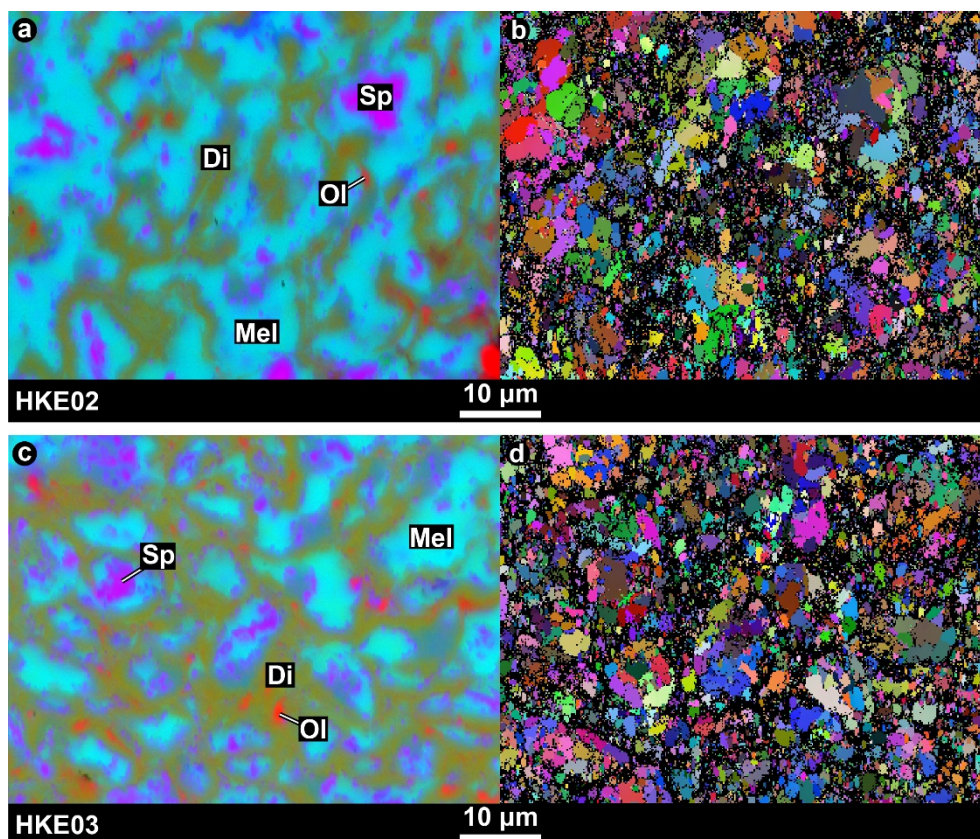
Figure 2. Representative textures of (a, b) *HKE02* and (c, d) *HKE03*. (a) Combined X-ray

elemental map in the area indicated by the yellow box in Fig. 1b denoting Mg (red), Ca

(green), and Al (blue). (b) Electron backscatter diffraction (EBSD) Euler map of the same

area shown in (a). (c) Combined X-ray elemental map in the area indicated by the yellow

box in Fig. 1c denoting Mg (red), Ca (green), and Al (blue). (d) Electron backscatter

diffraction (EBSD) Euler map of the same area displayed in (c). All the maps exhibit the

same field of view. Di, diopside; Mel, melilite; Ol, olivine; Sp, spinel.

677

678
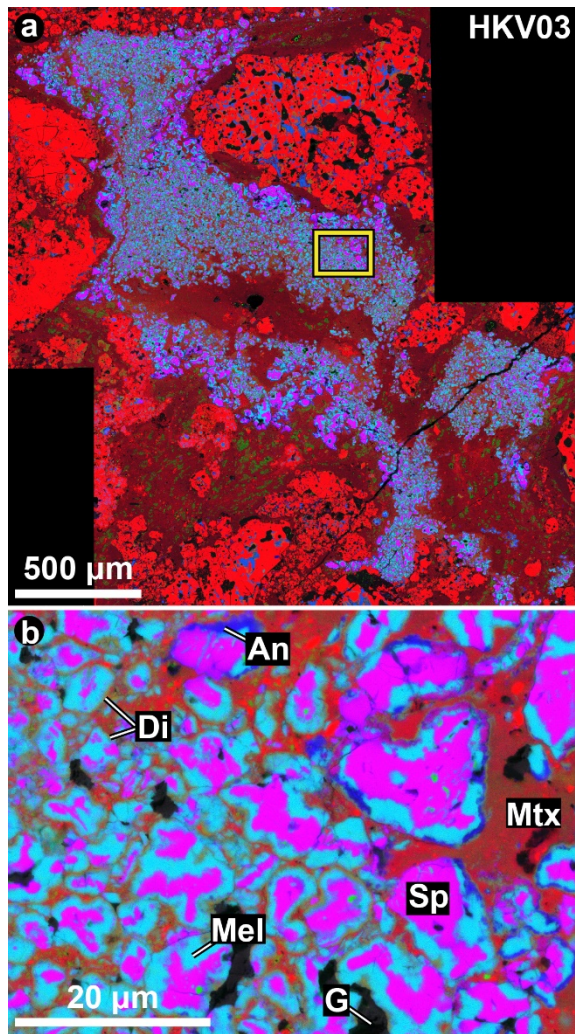
679 Figure 3. Combined X-ray elemental maps of fine-grained CAI *HKV03* from Vigarano

680 denoting Mg (red), Ca (green), and Al (blue). The yellow box in (a) indicates the area

681 shown in (b). An, Anorthite; Di, diopside; G, gold coating residues; Mtx, matrix; Mel,

682 melilite; Sp, spinel. Corresponding back scattered electron images are shown in Fig. S2.
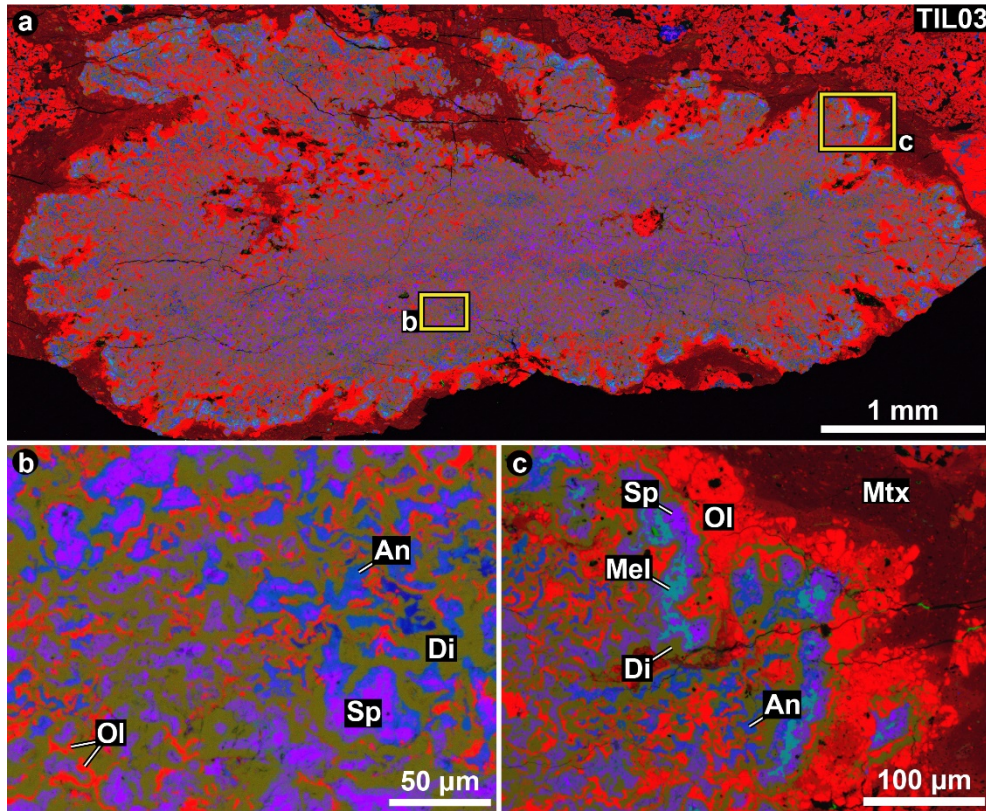
683

684
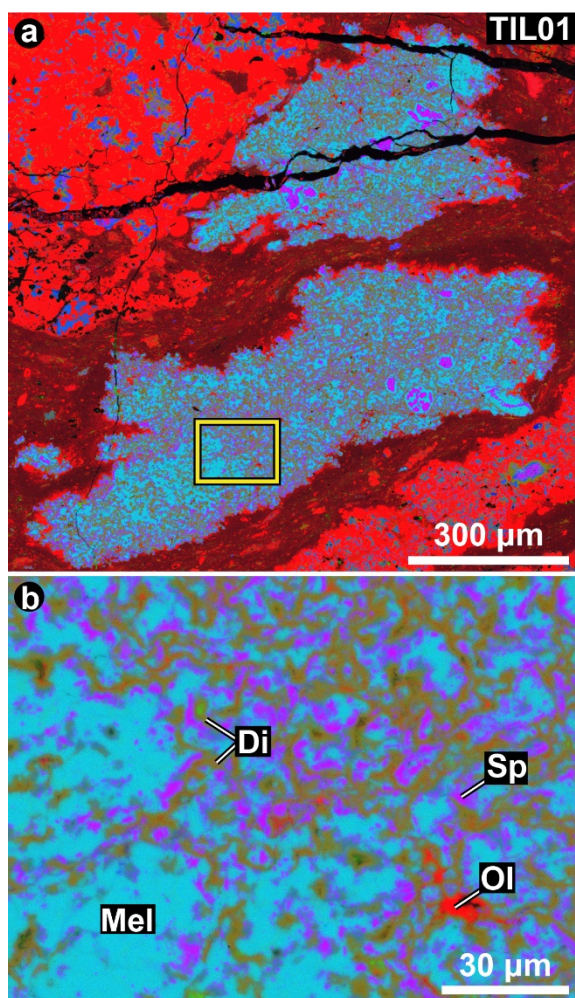
685 Figure 4. Combined X-ray elemental maps of fine-grained CAI *TIL01* from Theil

686 Mountains 07007 denoting Mg (red), Ca (green), and Al (blue). The yellow box in (a)

687 indicates the area shown in (b). Di, diopside; Mel, melilite; Ol, olivine; Sp, spinel.

688 Corresponding back scattered electron images are shown in Fig. S3.

689
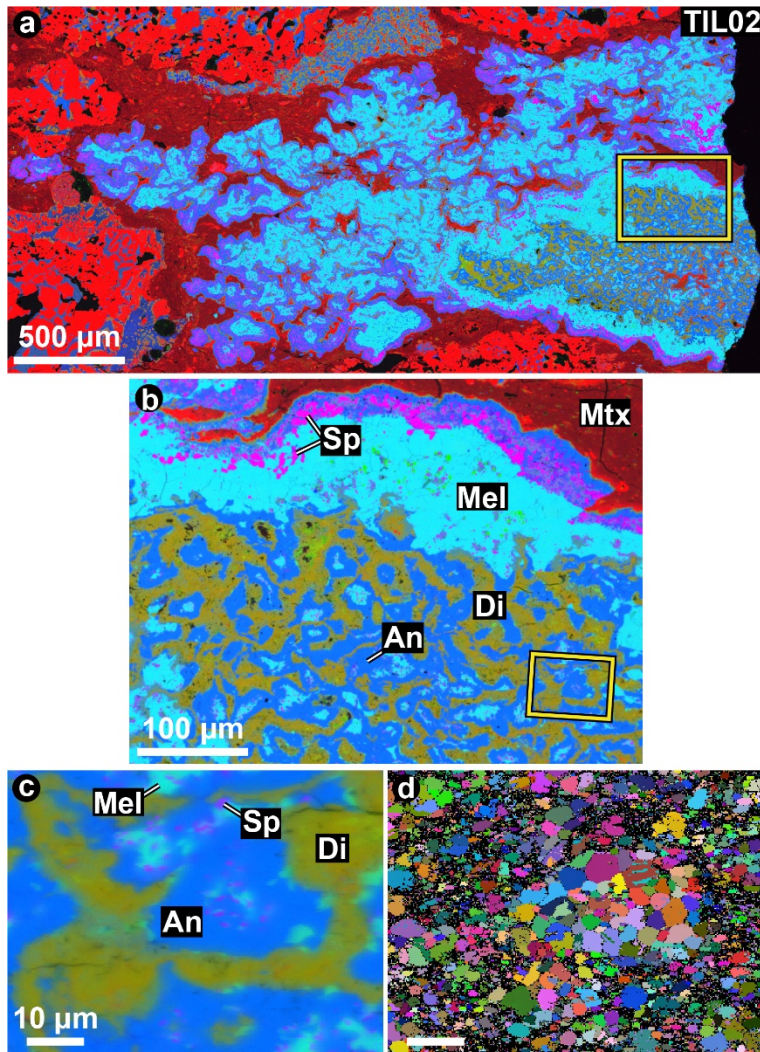
Figure 5. (a–c) Combined X-ray elemental maps of fine-grained CAI *TIL02* from Theil

Mountains 07007 denoting Mg (red), Ca (green), and Al (blue). The yellow box in (a)

indicates the area shown in (b). The yellow box in (b) indicates the area shown in (c). (d)

EBSD Euler map of the same area displayed in (c). An, anorthite; Di, diopside; Mtx,

matrix; Mel, melilite; Sp, spinel. Corresponding back scattered electron images are shown

in Fig. S4.

Figure 6. (a) Combined X-ray elemental maps of fine-grained CAI *TIL03* from Theil Mountains 07007 denoting Mg (red), Ca (green), and Al (blue). (b) Magnified elemental map of the area as indicated by box (b) in (a). (c) Magnified elemental map of the area indicated by box (c) in (a). An, anorthite; Di, diopside; Mtx, matrix; Mel, melilite; Ol, olivine; Sp, spinel. Corresponding back scattered electron images are shown in Fig. S5.
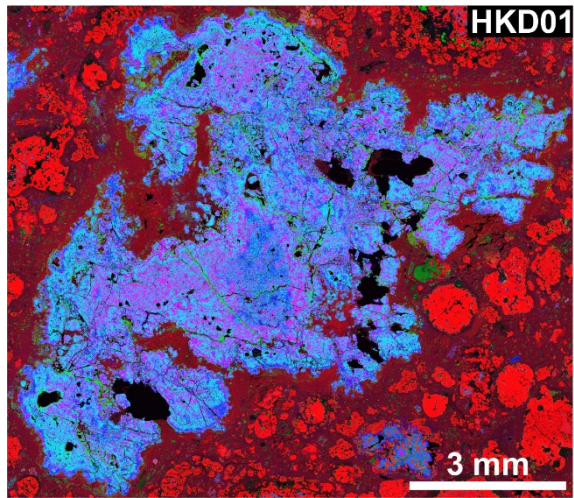
Figure 7. (a) Combined X-ray elemental map of fine-grained CAI *HKD01* from Northwest Africa 8613 indicating Mg (red), Ca (green), and Al (blue). A corresponding back scattered electron image is shown in Fig. S6.
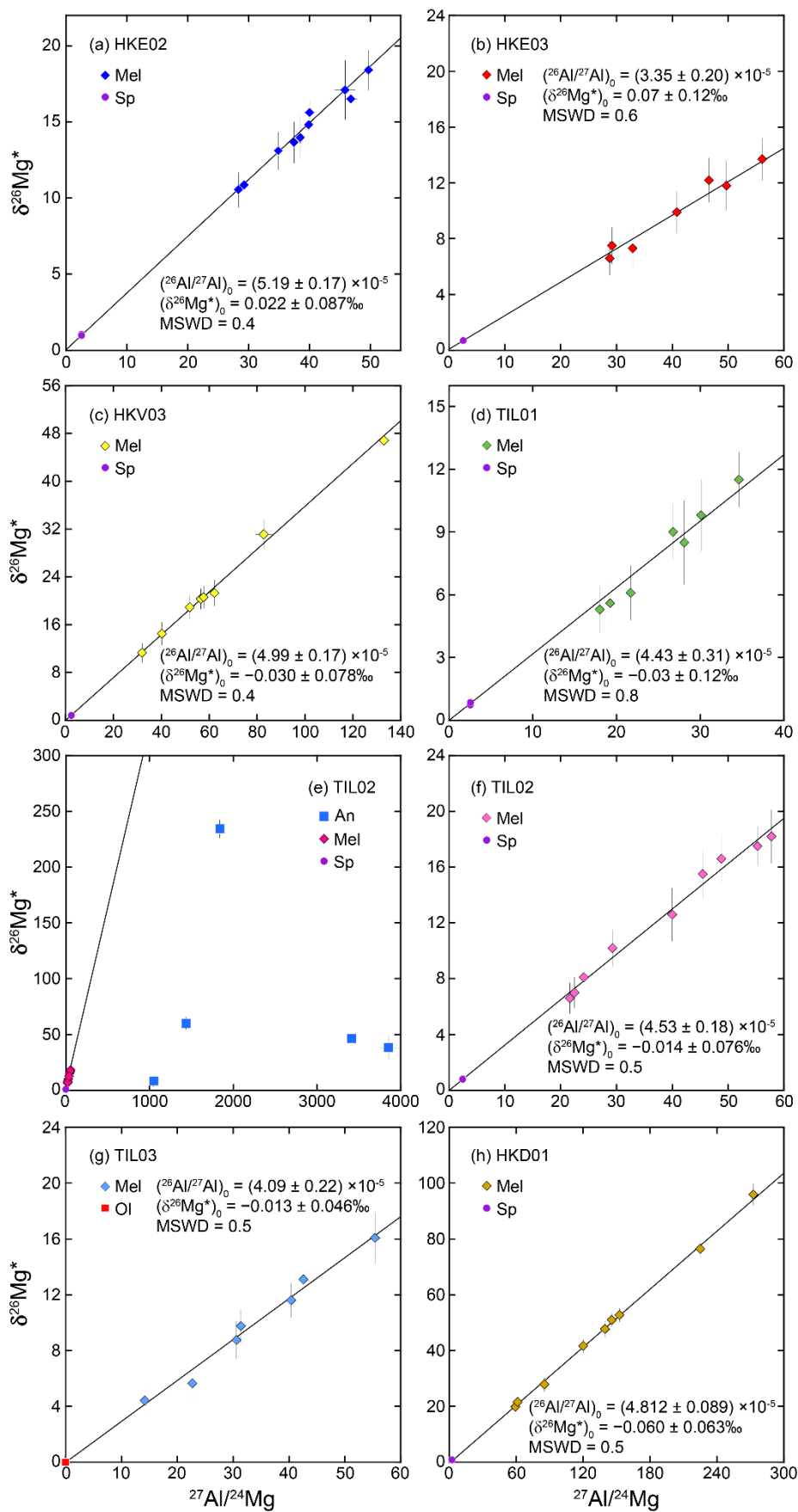
711　Figure 8. ^{26}Al–^{26}Mg mineral isochrons for fine-grained CAIs from reduced CV chondrites,

712　(a) *HKE02*, (b) *HKE03*, (c) *HKV03*, (d) *TIL01*, (e, f) *TIL02*, (g) *TIL03*, and (h) *HKD01*.

713　(f) shows data with low ^{27}Al/^{24}Mg ratio in (e). Al–Mg isotope data for (a) *HKE02* are

714　obtained from Kawasaki et al. (2019). Isoplot Model 1 (Ludwig, 2003) is used to fit

715　isochrons. Errors correspond to 2σ. Symbols without error bars exhibit errors smaller than

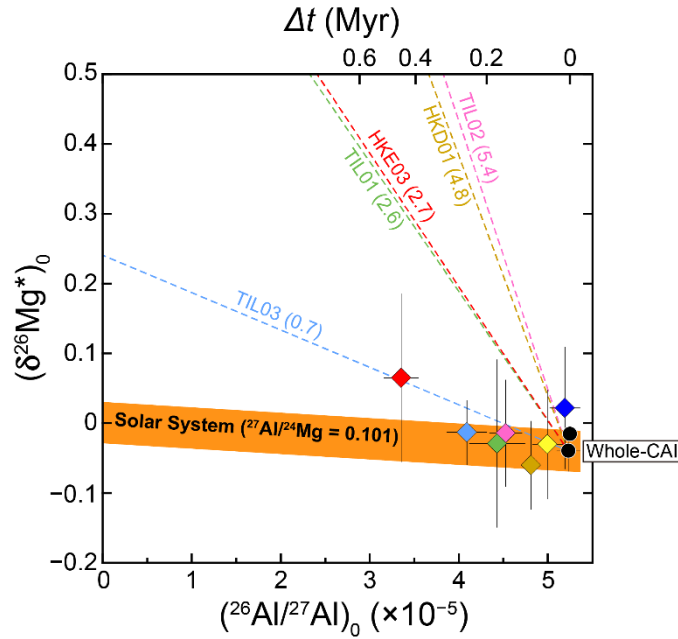716　their symbol sizes. An, anorthite; Mel, melilite; Ol, olivine; Sp, spinel.

717

718

719 Figure 9. Mg-isotope evolution of fine-grained CAIs from reduced CV chondrites. Mg-isotope

720 evolution curves starting from whole-rock CAI $(^{26}Al/^{27}Al)_0$ and $(\delta^{26}Mg^*)_0$ values (black circles,

721 Jacobsen et al., 2008; Larsen et al., 2011) are depicted by colored dotted lines for fine-grained

722 CAIs *HKE03* $(^{27}Al/^{24}Mg = 2.7)$, *TIL01* $(^{27}Al/^{24}Mg = 2.6)$, *TIL02* $(^{27}Al/^{24}Mg = 5.4)$, *TIL03*

723 $(^{27}Al/^{24}Mg = 0.7)$, and *HKD01* $(^{27}Al/^{24}Mg = 4.8)$, and by an orange-colored thick line for a solar-

724 composition gas $(^{27}Al/^{24}Mg = 0.101)$. If Al/Mg chemical fractionations for the fine-grained CAIs

725 occurred at the formation time of canonical CAIs, then Mg-isotopic compositions of the fine-

726 grained CAIs may have individually evolved by their bulk $^{27}Al/^{24}Mg$ ratios along the colored

727 dotted lines. Conversely, if the CAIs condensed from the solar-composition gas, then their Mg-

728 isotopic compositions would be plotted within the orange-colored thick line. Note that the Mg-

729 isotope evolution curves are drawn using the whole-rock CAI values by Jacobsen et al. (2008),

730 because the values reported by Jacobsen et al. (2008) entirely cover those of Larsen et al. (2011)

731 due to larger analytical errors. Colored diamonds correspond to inferred $(^{26}Al/^{27}Al)_0$ and

732 $(\delta^{26}Mg^*)_0$ values of the fine-grained CAIs. The $^{27}Al/^{24}Mg$ ratio of the Solar System is obtained

733 from Lodders (2003). Errors are 2σ.

734
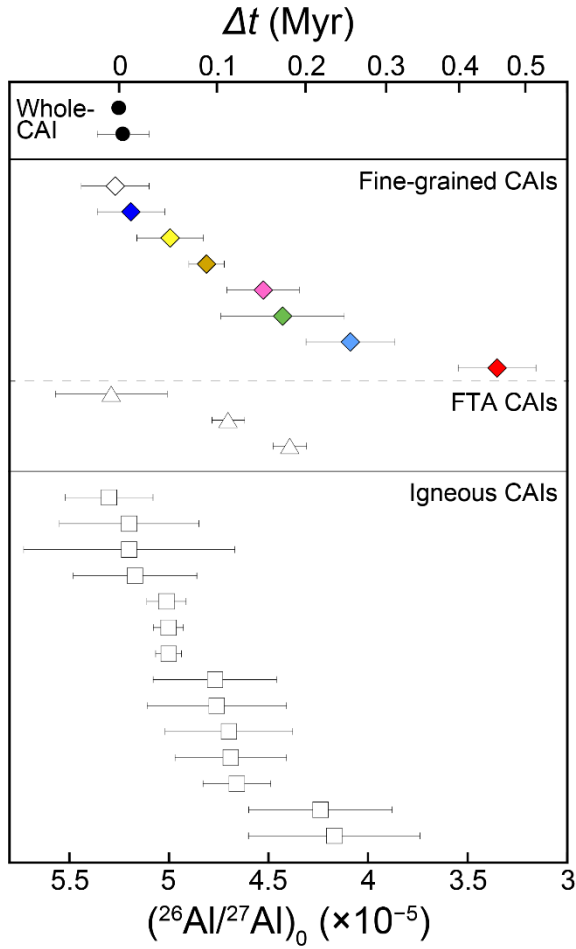
Figure 10. Variations in initial ^{26}Al/^{27}Al ratios for CAIs in CV chondrites as determined by high-precision mineral isochron studies. Initial ^{26}Al/^{27}Al ratios for fine-grained CAIs from MacPherson et al. (2010) (open diamond) and this study (colored diamonds) are shown for *L3536*, *HKE02*, *HKV03*, *HKD01*, *TIL02*, *TIL01*, *TIL03*, and *HKE03*, from top to bottom. Initial ^{26}Al/^{27}Al ratios for fluffy Type A (FTA) CAIs from the literature (open triangles, from top to bottom) are shown for *F8*, *V2-01*, and *HKE01* (MacPherson et al., 2012; Kawasaki et al., 2017, 2019). Initial ^{26}Al/^{27}Al ratios for igneous CAIs from the literature are shown for *E60*, *E64*, *SJ101*, *F9*, *USNM 3898*, *TS34*, *L3535*, *F4*, *V3137*, *4N*, *TS35*, *F1*, *F6*, and *ALVIN* (open squares, from top to bottom, Kita et al., 2012; MacPherson et al., 2012, 2017, 2018; Kawasaki et al., 2018). Whole-rock CAI initial

746    $^{26}Al/^{27}Al$ ratios (black circles) are from Jacobsen et al. (2008) and Larsen et al. (2011).

747   Errors correspond to 2σ.